

X-photon laser direct write 3D nanolithography

Edvinas Skliutas, Danielius Samsonas, Arūnas Čiburys, Lukas Kontenis, Darius Gailevičius, Jonas Berzinš, Donatas Narbutas, Vytautas Jukna, Mikas Vengris, Saulius Juodkasis & Mangirdas Malinauskas

To cite this article: Edvinas Skliutas, Danielius Samsonas, Arūnas Čiburys, Lukas Kontenis, Darius Gailevičius, Jonas Berzinš, Donatas Narbutas, Vytautas Jukna, Mikas Vengris, Saulius Juodkasis & Mangirdas Malinauskas (2023) X-photon laser direct write 3D nanolithography, *Virtual and Physical Prototyping*, 18:1, e2228324, DOI: [10.1080/17452759.2023.2228324](https://doi.org/10.1080/17452759.2023.2228324)

To link to this article: <https://doi.org/10.1080/17452759.2023.2228324>



© 2023 The Author(s). Published by Informa UK Limited, trading as Taylor & Francis Group



Published online: 03 Jul 2023.



Submit your article to this journal [↗](#)











View related articles [↗](#)



View Crossmark data [↗](#)

X-photon laser direct write 3D nanolithography

Edvinas Skliutas ^a, Danielius Samsonas ^{a,b}, Arūnas Čiburyš ^a, Lukas Kontenis ^b, Darius Gailevičius ^a, Jonas Berzinš ^b, Donatas Narbutas^c, Vytautas Jukna^a, Mikas Vengris ^a, Saulius Juodkasis ^{d,e} and Mangirdas Malinauskas ^a

^aLaser Research Center, Physics Faculty, Vilnius University, Vilnius, Lithuania; ^bLight Conversion, Vilnius, Lithuania; ^cInstitute of Theoretical Physics and Astronomy, Physics Faculty, Vilnius University, Vilnius, Lithuania; ^dOptical Sciences Centre and ARC Training Centre in Surface Engineering for Advanced Materials (SEAM), School of Science, Swinburne University of Technology, Melbourne, Australia; ^eWRH Program International Research Frontiers Initiative (IRFI) Tokyo Institute of Technology, Nagatsuta-cho, Midori-ku, Yokohama, Japan

ABSTRACT

Multiphoton photopolymerisation (MPP), also known as 3D nanoprinting, was studied using a wavelength-tunable femtosecond laser. The possibility of using any colour of the spectrum from 500 to 1200 nm with a fixed pulse width of 100 fs revealed an interplay of photophysical mechanisms more delicate than just two-photon photopolymerisation. An effective order of absorption, i.e. the X-photon absorption, as well as optimal exposure conditions were assessed for photosensitised and pure SZ2080TM pre-polymer. The tunability of wavelength greatly influenced the dynamic fabrication window (DFW), optimised conditions resulting in a 10-fold increase. Furthermore, a non-trivial energy deposition by X-photon absorption was noted with an onset of a strong lateral size increase at longer wavelengths and can be understood as due to reaching epsilon-near-zero conditions. Such a control over the voxel aspect ratio and, consequently, the photopolymerised volume, may boost 3D nanoprinting efficiency. Overall, the results reveal wavelength being an important degree of freedom to tailor the MPP process and, if optimised, benefiting broad applications in areas of micro-optics, nanophotonic devices, metamaterials and tissue engineering.

ABBREVIATIONS: MPP: multi-photon photopolymerisation; 2PA: two-photon absorption; CW: continuous wave; PI: photoinitiators; STED: stimulated-emission depletion; LOPA:ultralow one-photon absorption; DFW: dynamic fabrication window; RB: resolutionbridges; GDD: group-delay dispersion; SEM: scanning electron microscopy; CPD: criticalpoint drying; AR: aspect ratio; 2-BIT: two-beam initiation threshold; ENZ:epsilon-near-zero; O-FIB: optical-focused ion beam; ROI: regions-of-interest

ARTICLE HISTORY

Received 20 April 2023
Accepted 6 June 2023

KEYWORDS

Multi-photon photopolymerisation; laser direct writing; order of absorption; tunable wavelength; group delay dispersion; resolution bridges

1. Introduction

Multi-photon photopolymerisation (MPP) induced by ultrashort pulsed laser irradiation is commonly considered to happen via two-photon absorption (2PA) for so-called threshold materials as was revealed by S. Kawata and H.-B. Sun (Kawata et al. 2001). However, the number of photons N_p that are absorbed simultaneously to excite a molecule from the ground state to the excited state to start propagation of the chemical reaction depends on the absorption spectra of the photoresist and the wavelength λ of the excitation light. If λ of the incident light matches the absorption peak of the material – one-photon absorption occurs. If λ is twice longer than the absorption peak – two-photon absorption can be induced, and if λ is triple –

three-photon absorption is expected. However, the photopolymerisation process seems to be not so trivial. The lowest excited state might not be enough to initiate photopolymerisation, additional absorption mechanisms might be required for the photopolymerisation initiation and therefore the N_p can be a non-integer, especially for the intermediate λ . A similar phenomenon was observed in complex photosensitive systems where excitation to a triplet state is possibly causing a self-deactivation mechanism (Liaros and Fourkas 2021).

As the molecule excitation mechanism can be more complex than a simplified model of the ground-to-excited state transition, the so-called *effective* order of absorption n_{ef} should be taken into account, referring

CONTACT Edvinas Skliutas  edvinas.skliutas@ff.vu.lt  Laser Research Center, Physics Faculty, Vilnius University, Saulėtekio Ave. 10, Vilnius, LT-10223, Lithuania Supplemental data for this article can be accessed <http://dx.doi.org/10.1080/17452759.2023.2228324>.

© 2023 The Author(s). Published by Informa UK Limited, trading as Taylor & Francis Group

This is an Open Access article distributed under the terms of the Creative Commons Attribution License (<http://creativecommons.org/licenses/by/4.0/>), which permits unrestricted use, distribution, and reproduction in any medium, provided the original work is properly cited. The terms on which this article has been published allow the posting of the Accepted Manuscript in a repository by the author(s) or with their consent.

not to the total N_p involved in the transition, but to the effective N_p required to induce photoinitiation event. It is noteworthy that the discussion of n_{ef} pertains to the final geometrical size of the photopolymerised line, voxel, single feature *versus* pulse fluence or intensity. Hence, depending on n_{ef} , the photopolymerisation rate (voxel size per excitation) should scale as $I^{n_{ef}}$, where I is the light intensity. Moreover, the formation of a 3D photopolymerised structure is also dependent on the optical, thermal energy penetration depth, heat diffusion, thermal radiation, etc., which can also have a resonant nature and anisotropy guided by the scan direction, polarisation or applied external fields. Regardless of all those specific complexities, the effective absorption order parameter n_{ef} is of high technological relevance and is inherently connected to the energy deposition mechanism which drives photopolymerisation.

During the almost three decades since the first MPP publications (Maruo, Nakamura, and Kawata 1997), many scientific and commercial setups and machine tools were designed for different applications as well as for basic research. As a result, various types of laser sources were employed operating at diverse regimes: λ – 1064 nm (Perevoznik et al. 2019) (532 nm as second harmonic), 1030 nm (Malinauskas et al. 'Femtosecond Visible Light Induced' 2010) (515 nm (Merkininkaitė et al. 2022)), 800 nm (LaFratta and Baldacchini 2017) (400 nm (Miwa et al. 2001)), repetition rate R varies from 1 kHz to 100 MHz, pulse duration τ ranges from femtoseconds (fs) to nanoseconds (ns) (Stankevičius, Daugnoraitė, and Račiukaitis 2018) and even continuous wave (CW) has been reported (Mueller, Thiel, and Wegener 2014; Thiel et al. 2010). Uncertainty in the exact MPP mechanism arises not only due to λ (photon energy $h\nu$), but R and τ can modify the value of n_{ef} as it has a great influence on thermal effects (Baldacchini, Snider, and Zadoyan 2012), which in turn changes the photopolymerisation threshold (Obata, Lucas, and Sugioka. 2022). Regarding τ , it is worth mentioning, that it is usually provided as a laser source specification, without considering that focusing optics used in MPP has a great dispersion, meaning that τ at the sample is longer than declared, which in turn results in significantly different light intensity (spatio-temporal photon density) at the focus.

Moreover, plenty of monomers and photoinitiators (PI) are used to make photoresists for MPP (Kiefer et al. 2020), though some reports show photo-structuring without the usage of PI under specific conditions (Malinauskas et al. 'Mechanisms of Three-dimensional' 2010). The difference between photoresists is not only absorption spectra, but their viscosity, state of aggregation (liquid vs solid), pre-bake and post-bake conditions,

radical *versus* cationic chemical reactions, the absence or presence of oxygen inhibition and co-initiator, etc. All these factors can have minor or major impacts on how the photoinitiation is induced.

Both the laser source and the sensitivity of the materials used play important roles in the efficiency and applicability of MPP (Kiefer et al. 2020). To reduce feature size and spatial resolution, extraordinary equipment upgrades in combination with material engineering are needed. It was shown that a stimulated-emission depletion (STED) approach exploiting reversible photoenol activation with a photopolymerisation initiator allowed to polymerise of 60-nm-wide lines with 100 nm resolution (Mueller et al. 2017) or even finer individual features (Gan et al. 2013). However, in the last 10 years, a couple of new approaches were reported as lower-cost and simplified alternatives to MPP. Ultralow one-photon absorption (LOPA) was introduced in 2013 as a technique for curing photoresist SU8 with CW laser operating at $\lambda = 532$ nm (Do et al. 2013). Using LOPA, 3D woodpile structures with a period of 400 nm can be produced without the need for a post-bake step, however, extra low speeds (up to 3 $\mu\text{m/s}$) were used (Nguyen et al. 2016), making this method less efficient. To avoid 2-4 photon absorption to cure photoresist SU8 without a post-bake was investigated, where 1700 nm fs-pulses were used and concluded that in their setup thermal curing of the material had a larger impact than MPP (Marble, Marble, and Yakovlev 2020). In 2020, Zyla et al. used a compact monolithic picosecond (ps-)laser diode and achieved structural dimensions comparable to those generated by traditional MPP laser sources (Zyla et al. 2020). Wegener's group reported two-step absorption instead of MPP in 2021 (Hahn et al. 2021) where a real electron (defect) state instead of a virtual one was used for excitation. This required a special composition of photoresist prepared from common monomers and PI. This approach allowed the fabrication of rods with spacing below 300 nm using a CW semiconductor laser diode. A method employing layer-by-layer projection MPP ensures high-speed and continuous 3D printing. Related investigations were published sequentially in 2019 (Saha et al. 2019) and in 2021 (Somers et al. 2021). Research of new materials is important to improve MPP, e.g. new PIs were designed and synthesised for reducing the threshold of photopolymerisation and taking advantage of applications where only low laser power is available (Lunzer et al. 2022). Similarly, a new type of PI based on a broad dynamic fabrication window (DFW) was proposed (Ladika et al. 2022). Above mentioned techniques and approaches are mandatory for further improvements in MPP to

achieve great results in existing application areas or to expand it. Currently, MPP is employed in versatile manufacturing fields such as micro-optics (Ketchum, Alcaraz, and Blanche 2022) and diffractive optical elements (Sandford O'Neill et al. 2022), photonics (Blancher et al. 2020), microneedles arrays towards drug delivery applications (Mckee et al. 2022) and biomedicine (Fu et al. 2022), material structure engineering (Gailevičius et al. 2019), metamaterials (Münchinger et al. 2022), programmable materials (Zhang et al. 2019), multi-material microelectronics (Yang et al. 2023), microfluidics (McLennan et al. 2023), cryogenic applications (Peek et al. 2022) and tissue (Flamourakis et al. 2020) and biomimetic engineering (Zyla et al. 2022).

The aim to develop new methods to make MPP technology cheaper, more compact, and faster requires comprehensive investigation such as presented here. This research will give a better understanding of the photopolymerisation mechanisms and knowledge that can be applied to currently available MPP fs-pulsed regime laser systems (Skliutas et al. 2021) in photosensitised and non-photosensitised materials. Longitudinal and lateral sizes of photopolymerised 3D suspended lines (resolution bridges – RB) revealed complex power law dependencies with $Size \propto Power^\gamma$ showing wider power (energy) regions where γ defines the dominant energy deposition channel, which was found to be changing at specific average power for different wavelengths. The photo-excitation is validated for all λ and cannot be explained by just two-photon or three-photon absorption, thus is proposed to be femtosecond X-photon lithography.

The novelty of our research is that we have investigated line growth during photopolymerisation while tuning the wavelength but keeping the rest of the laser parameters constant: $R = 1$ MHz and $\tau = 100$ fs at the sample. This is essential, as various laser sources that are applied for MPP typically differ from each other by all three parameters (λ , R , τ) and make the results hard to compare. The demonstrated wavelength-tunability allows the studying of nano-scale and ultrafast chemistry processes such as nano-photopolymerisation/cross-linking. This can in turn be applied to the advanced additive manufacturing industry and gives important insights into the requirements of next-generation wavelength-tunable femtosecond lasers.

2. Methods

2.1. Experimental setup

The experiment was implemented using a CRONUS-3P laser source (Light Conversion, Vilnius, Lithuania). This

source was developed for advanced non-linear microscopy and extended to the UV–VIS range for this study. It provides μ J-level pulses down to 50 fs at repetition rates of up to 2 MHz and is tunable in the range from 400 to 1800 nm. This laser source provides tunable femtosecond excitation at the sample with an integrated group delay dispersion (GDD) control, ensuring optimal pulse duration at the sample. Pulse duration τ at the sample plane was measured with a CARPE microscopy autocorrelator (APE Angewandte Physik & Elektronik, Berlin, Germany). The excitation light was guided to the custom-made microscope setup and focused on the sample with a Zeiss Plan-Apochromat 100x 1.4 NA Oil objective. The sample was placed on a piezo-stage stack P-563 PIMars (Physik Instrumente, Karlsruhe, Germany) with the pre-polymer side down. The multi-axis piezo-stage assembly had a travel range of $300 \times 300 \times 300 \mu\text{m}$, thus it was mounted onto a motorised XY scanning stage 8MTF-75LS05 (Standa, Vilnius, Lithuania) with a travel range of $75 \times 75 \text{ mm}$. The objective was mounted on a motorised translation stage 8MT167-100 (Standa). An automated variable neutral density filter (VNDF) was used to control the average power P_{ave} , which was measured before the oil objective with power meter PD300 (Ophir, Israel) for $\lambda \leq 1100$ nm and 3A (Ophir, Israel) for $\lambda \geq 1200$ nm. The layout of the experimental setup is depicted in Figure 7.

2.2. Resolution bridges method

The Resolution Bridges (RB) method (DeVoe et al. 2003) was chosen as the basis for the experiment. As in the line-width method (Guney and Fedder 2016), the principle was to fabricate lines while increasing intensity (I) from the pre-threshold value until the onset of damage. Although the method we used is called Resolution Bridges, it is important to address, that in this work we are not investigating spatial resolution, which is a gap between two features (Fischer and Wegener 2013). Here we consider single feature size. In contrast to the line-width method, the supportive pillars were manufactured to maintain suspended lines after the developing process (see Figure 1 b). Each line was photopolymerised in a single-stage movement at a typical v of $100 \mu\text{m/s}$ to have single-voxel-wide features. To be able to measure the height of the lines, the offset from the monomer–substrate interface was set to $8 \mu\text{m}$. The dimensions, length \times width \times height, of a single pillar was $70 \times 25 \times 10 \mu\text{m}$. The entire object consisted of 6 pillars separated by $25 \mu\text{m}$ gaps from each other, resulting in total a width of $275 \mu\text{m}$. A sample scanning velocity of $500 \mu\text{m/s}$ was set for the photopolymerisation of pillars. The length of each line was set to $75 \mu\text{m}$ so that the line starts inside one

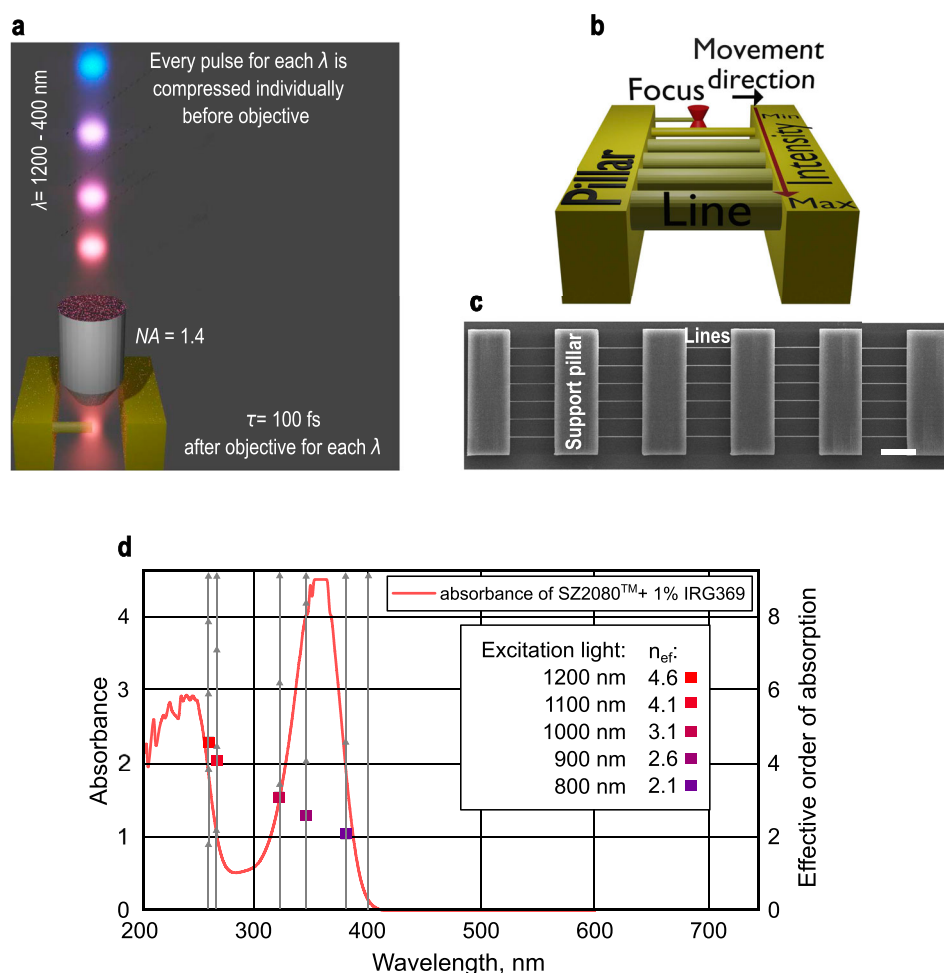


Figure 1. 3D resolution bridge (RB) printing and line analysis. **(a)** Illustration of GDD pre-compensated pulses propagating to the objective of $NA = 1.4$. After they pass the objective, $\tau = 100 \text{ fs}$ at each λ ; **(b)** Illustration of the RB method. The suspended single-voxel-wide lines are photopolymerised between support pillars, each row with different light intensity; **(c)** SEM image of the entire RB object with lines and support pillars. The white scale bar at the bottom right corner is $20 \mu\text{m}$; **(d)** Scheme representing calculated n_{ef} for used excitation light and their arrangement over measured absorbance spectra of photosensitised SZ2080TM. Grey vertical arrows visualise a number of photons for ground-to-excited state transition.

pillar and finishes in another, the standoff distance also ensured the line in the pillar gap was free of width fluctuations caused by stage acceleration. A total of 6 lines were fabricated in each gap between the pillars, resulting in 30 lines for the entire object. A distance of $10 \mu\text{m}$ was set between adjacent lines and was large enough to avoid proximity effects (Saha et al. 2017).

2.3. Materials

Experiments were conducted using photosensitised and pure SZ2080TM pre-polymer. Pure pre-polymer was purchased from The Foundation for Research and Technology – Hellas (FORTH; Heraklion, Greece), and photoinitiator 2-benzyl-2-dimethylamino-1-(4-morpholinophenyl)-butanone-1 (IRG369) was purchased from Sigma Aldrich. The photosensitised mixture was prepared by adding PI (1% w/w of pre-polymer) and stirring

with a magnetic stirrer until the PI dissolved. Before the experiment, pure and photosensitised SZ2080TM was kept at 4°C temperature. The photosensitised material was additionally placed on the magnetic stirrer for 10 min before drop-casting it on the substrate. Absorbance spectra of the photosensitised and pure pre-polymer were measured with a SHIMADZU UV Probe spectrophotometer and are shown in Figure 4(b).

2.4. Sample preparation and post-processing

Microscope coverslips (REF VBS638, Biosigma, Cona VE, Italy) were used as glass substrates for pre-polymer drop-casting and RB manufacturing. At first, the substrates were cleaned in an ultrasonic bath (EMAG Technologies, Mörfelden-Walldorf, Germany) in isopropanol for 20 min. Then the substrates were immersed in a mixture of isopropanol and

3-(trimethoxysilyl)propylmethacrylate (MAPTMS) (1:40 v/v) to enhance the adhesion of the photopolymerised object. After removing the substrates from the isopropanol/MAPTMS mixture, they were cleaned with acetone and air-dried. Finally, the pre-polymer was drop-casted onto the substrates and dried on a hot plate PZ 28-3T controlled by Programmer PR 5-3T (Harry Gestigkeit GmbH, Düsseldorf, Germany). The drying program was set as follows: 40 min at 40°C, 40 min at 70°C and 40 min at 90°C.

After the RBs were manufactured, the samples were placed in a Petri dish with 4-methyl-2-pentanone for development for 30 min to dissolve uncured pre-polymer, then removed and placed in the second Petri dish with the same solvent for another 30 min. A critical point dryer (CPD) K850 (Quorum Technologies, East Sussex, UK) was used to dry the samples. The samples were sputtered with a 10-nm silver layer employing a rotary pumped coater 150R S (Quorum Technologies, East Sussex, UK).

2.5. Sample characterisation

Samples were characterised using a scanning electron microscope (SEM) Prisma E (Thermo Fischer Scientific, Eindhoven, The Netherlands). The recorded images were stored in 8-bit TIFF with an intensity range of (0, 255) counts. Samples were observed from the top for line width measurement and at a 45° angle for height measurement.

2.6. Analysis of the SEM images

The obtained SEM images were processed with Python programming language to determine the average line width and height of the photopolymerised lines. At first, DS9 software (Joye and Mandel, 2003) was used to visually inspect SEM images of the lines, define regions-of-interest (ROI) around each line and enumerate them (see Figure S1 in *Supplementary* file). Then, a box of ≈ 1000 columns \times 200 rows of pixels was cut for analysis at each photopolymerised line position and converted to binary by applying a threshold for pixel values. The pixels representing the photopolymerised lines were set to 255 and the background to 0. The threshold to binarise the images was chosen manually for each collection of images due to variable SEM scanning properties: chosen electron energy and image resolution – pixel scale. To ensure that imaging conditions do not influence line-width estimation, each binarised image of the line was verified by eye by comparing it to the original SEM image. Next, the vertical boundaries of each line were determined as pixel value changes

from 0 to 255 (top boundary) or from 255 to 0 (bottom boundary). Scanning from top to bottom of the defined ROI, the value of every pixel in every column was compared with the following four adjacent pixels to be certain that the line boundary was found while ignoring local pixel-to-pixel noise, this gives us a robust edge detection of the line. The difference between the top and bottom boundaries gives us a vertical extent of the line (computed as mean and standard deviation). Here we report the mean value of the measured vertical extent, which corresponds to the width of the line for perpendicular SEM images and the height of the line for 45° rotated SEM images. Pixels were converted to μm using a factor $\mu\text{m}/\text{pixel}$ from the SEM image metadata. The height was multiplied by $\frac{1}{\sin 45}$ to calculate a real line height instead of a projection.

2.7. Calculations and formulation

Peak power (P_{peak} , Equation 1) and pulse energy (E , Equation 2) were calculated by dividing P_{ave} by the pulse duration τ and repetition rate R .

$$P_{\text{peak}} = \frac{P_{\text{ave}}}{R\tau}, \quad (1)$$

$$E = \frac{P_{\text{ave}}}{R}, \quad (2)$$

To estimate fluence (F , Equation 3) and intensity (I , Equation 4), E and P_{peak} were divided by the focal area $\frac{\pi r^2}{2}$, where r – the Airy radius (Equation 5). Also, the transmittance T of the objective was measured experimentally and included in calculations.

$$F = \frac{2TE}{\pi r^2}, \quad (3)$$

$$I = \frac{2TP_{\text{peak}}}{\pi r^2}, \quad (4)$$

$$r = \frac{0.61\lambda}{NA}, \quad (5)$$

Equation 6 describes Abbe's diffraction formula for axial resolution in which n is the refractive index of SZ2080™ which is equal to 1.5 (Ovsianikov et al. 2008).

$$l = \frac{2\lambda n}{NA^2}, \quad (6)$$

DFW was calculated as the difference between the intensities of optical damage (I_{dam}) and photopolymerisation threshold (I_{pol}), normalised to the I_{pol} (Equation 7). Basically, it defines, what intensity/average power values are suitable for the fabrication to avoid optical damage keeping the photopolymerisation threshold as the

reference point.

$$DFW = \frac{I_{\text{dam}} - I_{\text{pol}}}{I_{\text{pol}}}. \quad (7)$$

The values for I_{dam} and I_{pol} were assessed from the brightfield live imaging during photopolymerisation and later specified from SEM images.

The data of voxel lateral and longitudinal growth was approximated using Equations (8) and (9), respectively (Juodkazis et al. 2005).

$$\text{Lateral} = 2r_0 \sqrt{\frac{2}{n_{\text{ef}}} \ln \frac{I}{I_{\text{pol}}}}, \quad (8)$$

$$\text{Longitudinal} = 2z_r \sqrt{\left(\frac{I}{I_{\text{pol}}}\right)^{\frac{1}{n_{\text{ef}}}} - 1}, \quad (9)$$

Parameters r_0 and z_r were fixed for each λ , while parameters I_{pol} and n_{ef} – effective order of absorption – were set as a variable with initial values. The Rayleigh length is denoted z_r (Equation 10).

$$z_r = \frac{n\pi r_0^2}{\lambda}. \quad (10)$$

3. Results

The experiment was designed to investigate MPP in a wide λ range from 400 to 1200 nm every 100 nm while maintaining a constant τ of 100 fs at the sample for each λ with $R = 1$ MHz and writing velocity $v = 100$ $\mu\text{m/s}$. The chosen velocity is relatively slow comparing with the ones used for the rapid prototyping – tens of mm/s (Liu et al. 2019; Zhang et al. 2022). Though it is possible to achieve such velocities in SZ2080TM with oscillator and amplified system (Butkus et al. 2022; Jonušauskas et al. 2019), 100 $\mu\text{m/s}$ is still common writing velocity where high precision or investigation is needed (Lemma et al. 2017). Figure 1(a) depicts different λ pulses, which are pre-compressed with group-delay dispersion (GDD) control to compensate for high-dispersion caused by focusing optics. This control is mandatory when short λ and τ are used. There was no possibility to measure τ below 700 nm due to limitations of the autocorrelator which was used, but an estimation of dispersion-inducing components and GDD control allowed us to achieve the shortest possible τ at that regime.

Figure 1(b) represents a scheme of printing of RB and Figure 1(c) shows a top-view scanning electron microscopy (SEM) image of photopolymerised RB model after development in solvent and critical point drying (CPD) to avoid possible mechanical distortions due to capillary forces. These particular bridges were

fabricated using 900 nm wavelength in a photosensitised pre-polymer. Figure 1(d) – a visualisation of the assessed n_{ef} over absorbance spectrum of photosensitised pre-polymer is provided. The points demonstrate where the absorption for each excitation λ should occur. All the values of n_{ef} parameter can be found in Table S1 at *Supplementary file*.

The width and height of the photopolymerised lines were measured from SEM images. The estimated voxel's lateral and longitudinal dimensions at different average power for different λ in photosensitised and pure SZ2080TM pre-polymer are presented in Figure 2. Data at 400 nm is not presented due to two reasons: (1) the photopolymerisation was excited via one-photon in pre-polymer with PI, thus RB structure was photopolymerised solid having no lines and (2) the photopolymerised RB in pure pre-polymer did not survive development and CPD treatments. By comparing the Figure 2 graphs it is seen that the addition of the 1% PI IRG369 has allowed photopolymerisation within a broader λ range (500–1200 nm) than without PI (only up to 1000 nm). This 200 nm difference originates from the absorption spectra (Figure 4 b), where it is clearly seen that both photosensitised and pure pre-polymer have peaks at ≈ 245 nm, meanwhile the photosensitised has a second peak at ≈ 360 nm. It gives an additional 115 nm of linear absorption, due to which efficient non-linear absorption can be induced at longer λ .

The fits by Equations (8) and (9) (Section 2.7) aimed to capture the evolution of voxel/line size at the lowest powers and the line is then extended to the maximum power of the pulse. This qualitative fit defines the n_{ef} process order parameter linked to the energy deposition mechanisms as discussed above. The log–log presentation is chosen to visualise the quality of the fit at a fast-changing part of the size evolution as well as to spot global tendencies of the slope γ changes. The n_{ef} value can be understood as a local parameter since it defines how much Gaussian-like intensity envelope delivers energy deposition above the photopolymerisation threshold. There is a clearly discernible departure from the fit at large pulse energies/powers which can be understood as global parameters where the γ slopes evolve from sub-linear to super-linear $\gamma > 1$. The possible mechanism behind such scaling is discussed in more detail further (Section 4).

The growth rate of the lateral and longitudinal size of the voxel with the increase of the laser power is different for each λ regardless of the presence of PI. In all the cases, we have observed a relatively good match between the analytical curve defined by n_{ef} and experimental data for the voxel longitudinal size evolution. However, the lateral size of the voxel fits nicely only

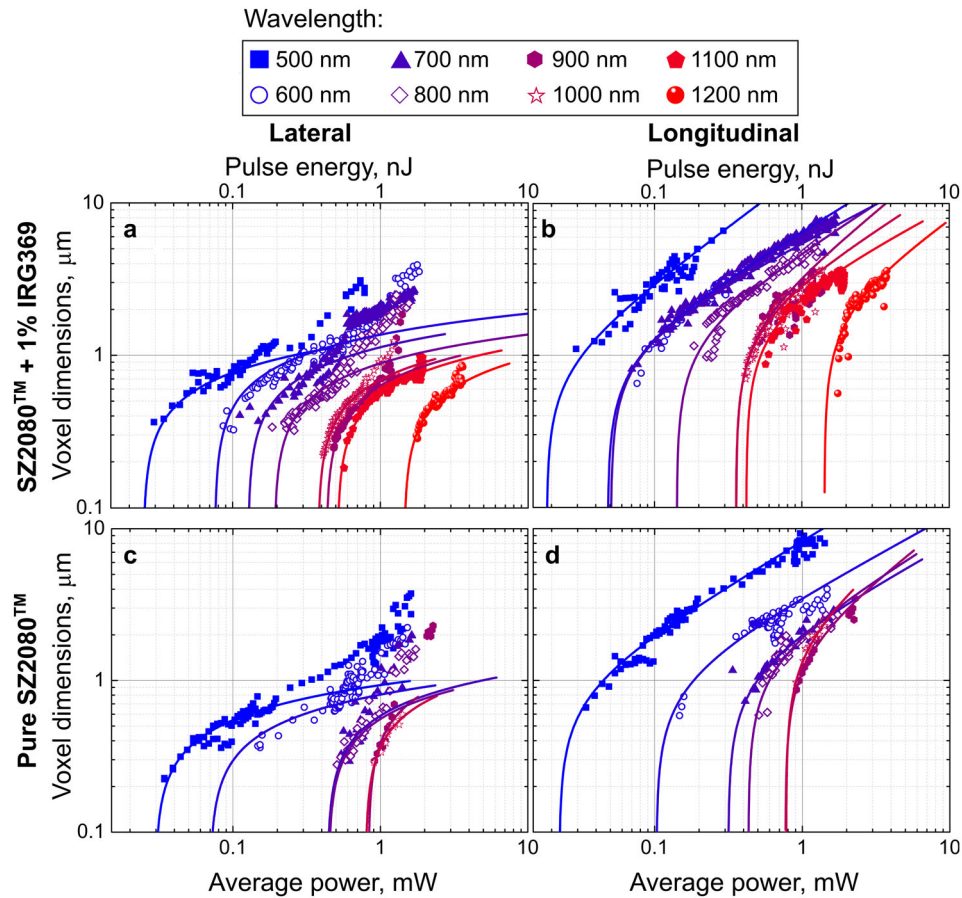


Figure 2. Voxel dimensions dependence on average power at different λ : **(a)** lateral voxel size in photosensitised pre-polymer; **(b)** longitudinal voxel size in photosensitised pre-polymer; **(c)** lateral voxel size in pure pre-polymer and **(d)** longitudinal voxel size in pure pre-polymer. Solid lines are approximations with Equations (8) and (9) for lateral and longitudinal voxel growth. Average power is multiplied by measured objective transmittance for each λ .

when they are produced with low laser power. At higher powers, the departure from the analytical curve signals a different energy deposition method for photopolymerisation initiation and consequently changes the voxel size. The voxel lateral size growth with the laser power nicely fits with the linear power scaling (global scaling $\gamma = 1$, i.e. $Size \propto P_{ave}^\gamma$). The longitudinal voxel dimensions fit the analytical curve better for the entire wavelength range and laser powers. This can be explained by the different intensity distributions in lateral and longitudinal sections in the focus. The Gaussian-like intensity decreases radially as $\propto e^{-r^2}$ while longitudinally as $\propto e^{-z}$, where z is the dimension along pulse propagation. For the same energy deposition, the longitudinal dimension is less sensitive to intensity gradient in absorption as compared with the lateral (along the radius r of the focal spot). Despite the fact that data for the longest λ were not obtainable for pure SZ2080™ due to the fast growth of the lateral size (an explosive-like energy deposition) the same trends were observed for shorter wavelengths and even the linear lateral voxel growth with

global $\gamma = 1$ parameter was observed, showing the intensity distribution in the focal region playing a major role in the voxel size trends.

It is noteworthy that wider and longer lines were obtained using visible light rather than infrared, which is opposite to the expectation considering the diffraction argument where the diameter of the focal spot (Equation 5) increases with the increase of wavelength. Apparently smaller voxels can be produced due to the higher order of absorption (or smaller cross-section) at longer λ and can compensate for the beam diameter increase. Figure 3(a) shows the smallest measured lateral and longitudinal voxel dimensions. The minimal line-width fluctuated between 200 and 400 nm within the entire λ range for both photosensitised and pure pre-polymer. Line height varied more – from 0.5 to 1.25 μm . Thus a clear trend of the smallest achievable voxel size was not determined. Also, the refractive index is not the same within investigated wavelengths range (Dottermusch et al. 2019), thus this parameter could have a minor effect on voxel dimensions

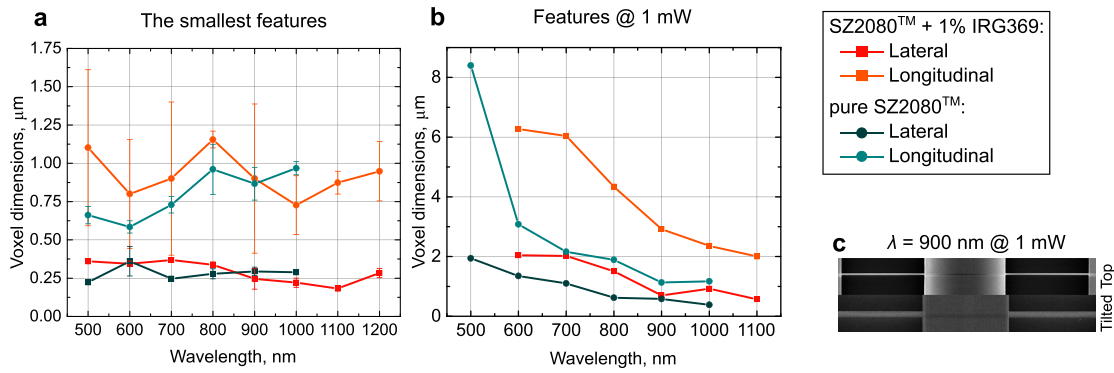


Figure 3. Voxel dimensions: smallest and obtained at fixed power: **(a)** measured smallest lateral and longitudinal voxel dimensions at each λ ; **(b)** voxel dimensions dependence on λ , when $P_{\text{ave}} \approx 1 \text{ mW}$; **(c)** an example, representing the same lines from top and angled perspectives. Manufactured using 900 nm.

according to Equation (6). Figure 3(b) shows how the voxel size evolved at fixed $P_{\text{ave}} = 1 \text{ mW}$. For both pre-polymers, lateral and longitudinal dimensions of a voxel decreased for longer λ . 500 nm is a special case when a sudden increment of line-height was observed. This augmentation is related to increased energy deposition when optical damage begins (around 1 mW in both pre-polymers). From experimental data, it was estimated that voxel longitudinal dimensions at 500 nm can exceed $8 \mu\text{m}$, which was RB writing depth from the substrate. In this case, the lines were attached to the substrate and were taller than the supportive columns. Because of the arrangement of the lines, they overlapped in SEM images despite the tilt angle. Due to this reason, the data for photosensitised pre-polymer at 500 nm was not acquired and is not depicted on the graph. Figure 3(c) represents SEM images of the same lines manufactured with $\lambda = 900 \text{ nm}$ from top- and tilted-view.

Figure 4(a) shows the DFW graph where the widest DFW was obtained at shorter λ and dramatically decreased by ≈ 28.6 times in the infrared spectral range. The highest DFW values were calculated for 500 nm and 700 nm when PI was used. Interestingly, the absence or presence of PI changed DFW only 1.2 times for 500 nm but 16 times for 700 nm. It can be said that the addition of 1% wt. of IRG369 not only expanded the λ range suitable for photopolymerisation but also had an influence on controlling the DFW for each λ individually. Next to SZ2080TM, considering other organic and hybrid materials it is expected that using femtosecond pulses various wavelengths can be exploited to initiate the MPP process, disregarding the usage of PI, yet strongly influencing the DFW. The reason why PI affects DFW is not only higher absorption at the visible spectrum but also ionisation energy. Photoinitiators require less energy to be excited, thus photopolymerisation thresholds are lower compared

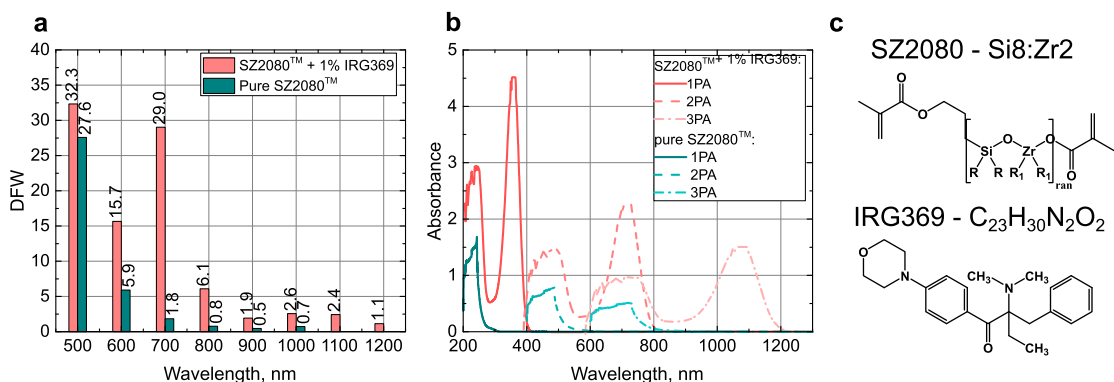


Figure 4. Dynamic Fabrication Window and absorbance spectra: **(a)** DFW dependence on λ in photosensitised and pure pre-polymer; **(b)** absorbance spectra of photosensitised and pure SZ2080TM pre-polymer. Photosensitised pre-polymer has two peaks of linear absorption (1PA) at 245 and 360 nm. Pure pre-polymer has one linear absorption peak at 245 nm (depicted as normalised to the peak of photosensitised pre-polymer). Non-linear absorption (two/three-photon (2PA and 3PA)) is depicted by multiplying the x-axis of the linear absorbance spectrum and dividing the y-axis by two and three times, respectively; **(c)** chemical formulas and structures of SZ2080TM and IRG369 (Gailevičius et al. 2019).

to pure monomer. This case was more detailed explained in previous publication (Samsonas et al. 2023). Additionally, different PIs are capable to generate different amounts of free radicals. Thus using high-efficiency molecules such as 7-diethylamino-3-thenoyl-coumarin (Vyatskikh et al. 2018) could alter not only the *DFW* but increase voxel lateral and longitudinal dimensions.

Also interesting was the variation of the aspect ratio (*AR*) of the generated voxel size within the *DFW* at different λ . *AR* was defined as a ratio of longitudinal to lateral voxel dimensions. Obtained graphs are depicted in Figure 5. The *AR* was found to behave similarly as reported previously (DeVoe et al. 2003; Sun et al. 2003): *AR* rapidly increased or had an initial high value at the very start region of *DFW*, and then tended to

decrease or stay constant until the damage intensity I_{dam} was reached. At low powers, the voxel developed faster in a longitudinal direction than in the lateral, which is expected based on the Equations (5) and (6) and was observed for every λ within the investigated range for both pre-polymers. With increasing P_{ave} , the lateral and longitudinal growth speeds remained constant resulting in constant *AR*. However, for $\lambda = 700 - 1000$ nm in photosensitised pre-polymer, and for $\lambda = 700 - 900$ nm in pure pre-polymer, a further increase of power caused a decrease of *AR*, implying that the growth in the lateral direction had increased. As no photopolymerised lines and pillars were obtained with $\lambda = 1100$ nm and 1200 nm in pure pre-polymer, no-photopolymerisation and optical damage zones were marked on the graphs.

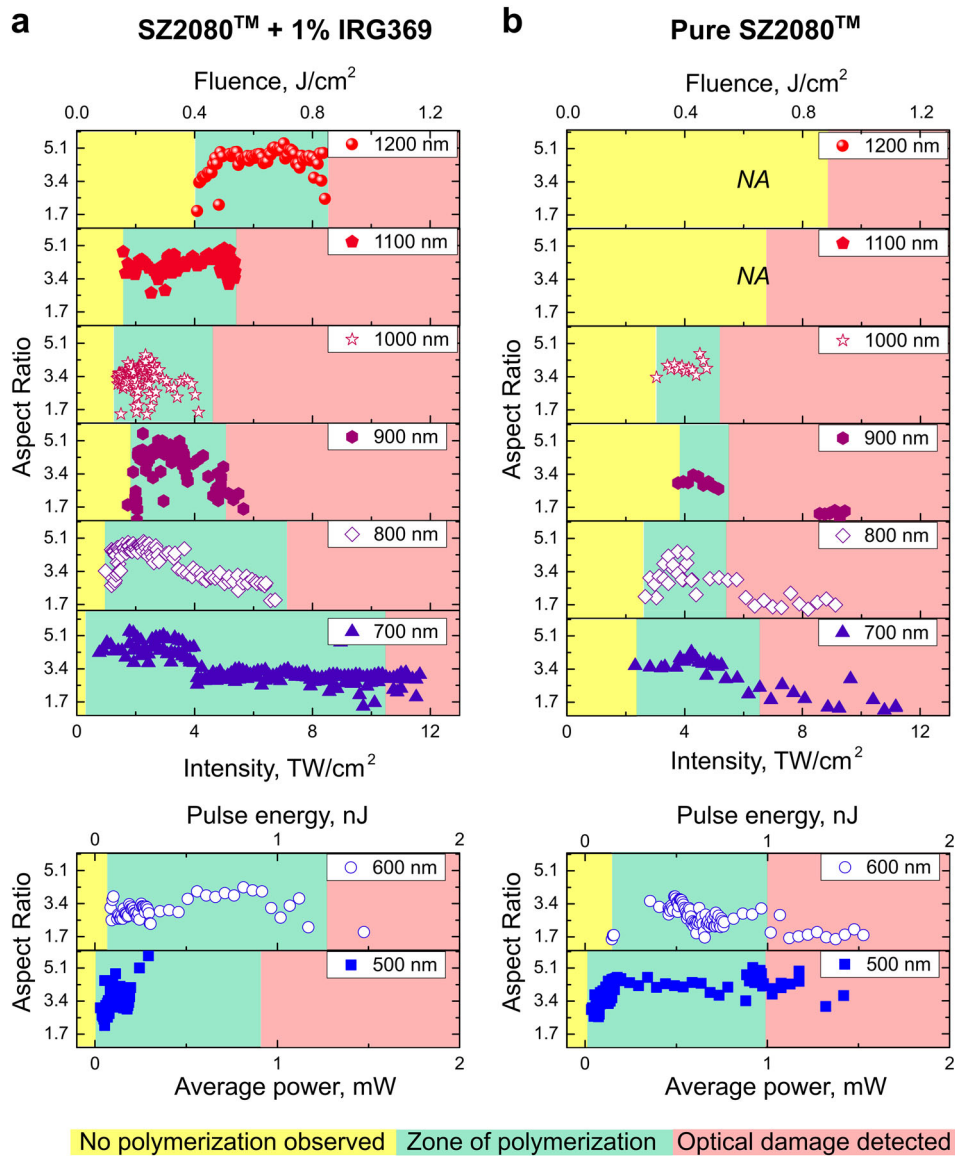


Figure 5. Dependence of aspect ratio on average power/intensity for different λ : (a) *AR* in photosensitised pre-polymer and (b) *AR* in pure pre-polymer. The coloured background in the graphs marks non-photopolymerisation, photopolymerisation and optical damage zones.

4. Discussion

The voxel formation was a high-interest research field regarding the MPP technique. Two main approaches were considered for it: a single-voxel method and a line-width method. The former method allows observation of a single voxel, which is the smallest building unit in MPP (Hahn et al. 2020). The width, height and shape of the voxel can be assessed by varying an exposure dose. However, to make 3D objects, sample translation or beam scanning is applied, thus making a line the main and practical building unit in MPP. Hence, line formation at varying exposure dose by changing P_{ave} or scanning speed v was found to be a better proxy. The lines can be formed in two ways: attached to the substrate, or suspended as in the RB method. When attached, the impact of shrinkage during development is reduced. Using this method only the line width is usually assessed but height estimation is also possible (Guney and Fedder 2016). By making suspended lines, both width and height are easily assessed. Although AR can also be calculated, this parameter is less common in the literature (Guney and Fedder 2016; Sun et al. 2003; Williams et al. 2017). Line-height can be partly influenced by spherical aberration which depends on focusing numerical aperture NA , depth of focus and refractive indices mismatch (Horváth, Ormos, and Kelemen 2017). In this study, care was taken to minimise spherical aberration by $\sim 8 \mu\text{m}$ RB writing depth.

Techniques other than measuring voxels or line dimensions were developed to investigate MPP. For example, the kinetics of photopolymerisation (Mueller et al. 2014), the exposure-time method (Yang et al. 2019), the repetition rate method (Baldacchini, Snider, and Zadoyan 2012), and the two-beam initiation threshold (2-BIT) method (Tomova et al. 2016) were dedicated to assessing the n_{ef} of MPP. All the aforementioned methods, including the line-width method, are discussed in a recent review by Liaros and Fourkas (Liaros and Fourkas 2021). They highlight that knowing n_{ef} is mandatory to create new and enhanced photo-reactive materials, however, every technique is limited by certain conditions and thus not suitable for a reliable determination of n_{ef} . Recently, Johnson et al. provided a detailed theoretical model to explain physical processes in MPP when self-deactivation – inhibition due to absorption in triplet state – is occurring, and applied it to the experimental results of the line-width model to determine n_{ef} (Johnson and Yijie Chen 2022). They also showed that n_{ef} can acquire higher values as self-deactivation can cause an increase in the molar extinction coefficient.

The application of the line-width method for the determination of n_{ef} is broadly debated in the MPP community. The main question was whether it is at all possible to assess n_{ef} . Equations (8) and (9) were used to determine power laws of photopolymerisation (Juodkasis et al. 2005), however, another idea that n_{ef} cannot be determined from the line-width was argued (Fischer et al. 2013). By comparing results obtained for the photoresist with IRG369 (PI) employing a laser system operating at $\lambda = 800 \text{ nm}$, $R = 1 \text{ MHz}$ and $\tau = 150 \text{ fs}$ (Fischer et al. 2013) with results of our research at 800 nm, both approximations – no matter whether n_{ef} was included in the model or excluded – fitted the data well at the low pulse energies. As mentioned before, we made approximations on the lateral voxel dimensions including only the lines thinner than 800 nm. Other authors (Fischer et al. 2013) have applied a similar approximation only for the lines up to 450 nm in thickness. A linear voxel growth at R from 0.5 to 1 MHz using ps pulses was observed (Malinauskas, Danilevičius, and Juodkasis 2011). The presence of thermal accumulation was assumed to cause this behaviour.

We have obtained n_{ef} parameter values from the fit results. Using pre-polymer with IRG369, the best approximations were obtained for 1200 and 1100 nm, yielding the value of $n_{ef} = 4.6$ and 4.1, respectively. Under such conditions, we should expect absorption to be around 260–270 nm, which is close to the absorption peak of the photosensitised pre-polymer at 245 nm (Figure 1 d). For $\lambda = 1000$ and 900 nm, n_{ef} was calculated to be 3.1 and 2.6, resulting in absorption at ≈ 320 –345 nm, which comes from the second absorption maximum in the photosensitised system at 360 nm. While n_{ef} for 800 nm was assessed to be 2, resulting in absorption at 400 nm, which according to the measured spectra has low absorbance. This result agrees with the 2-BIT method measurements, where 800 nm was absorbed with an order of non-linearity of 2 for IRG369 (Tomova et al. 2016). The same result was shown earlier by applying the exposure-time method (Fischer et al. 2013). For shorter λ , the value of the n_{ef} parameter was assessed to be even smaller: 1.2 for 700 nm, 0.9 for 600 nm and only 0.8 for 500 nm. It has been reported, that PI, which has a strong absorption at 260–280 nm, absorbed 800 nm irradiation via a 3-photon process (Tomova et al. 2016). In our case, a pure pre-polymer had a comparable spectrum. Non-linearity of only 2.5 was assessed from the best fit. For 900 and 1000 nm, n_{ef} was 1.6 and 2.7, respectively. Higher non-linearity would be expected for this λ range, but such a discrepancy can be explained by a narrow DFW at 800, 900 and 1000 nm, as not a sufficient amount of data was acquired for a better fit. A narrow DFW is a drawback

in MPP technology, as the photophotopolymerisation threshold and optical damage threshold values are close, thus making the photopolymerisation process less controllable.

A comprehensive work on the determination of n_{ef} using the line-width method was performed by Williams et al. (2017). They conducted the experiment in epoxy photoresist SU8 using an acid-based photosensitiser PAG, which makes the research a lot different from our work as photopolymerisation mechanisms and post-treatment were distinctly different: cationic *versus* radical, post-bake *versus* no post-bake. Additionally, it is known that epoxy photoresists do not suffer from shrinkage as radical ones do. However, some similarities in experiment design $\lambda = 800$ nm, $\tau \approx 100$ fs, $R = 1$ kHz or 76 MHz were present. Only the line width was calculated from the suspended lines, but the authors have varied v in a wide range from $6 \mu\text{m/s}$ to $800 \mu\text{m/s}$. They also found that Equation (8) (not including n_{ef}) did not fit wider lines well, thus only lines thinner than 700 nm were used for the analysis. By plotting a logarithmic dependency of photopolymerisation threshold power on v , the authors have determined $n_{\text{ef}} = 3$ for 800 nm excitation. An investigation of n_{ef} *versus* λ was performed by combining Z-scan (500 – 800 nm) and line-width (725 – 875 nm) methods. Z-scan gave the values of n_{ef} from 1.8 at 3.2 , and the line-width method revealed that n_{ef} increased from 2.2 at 700 nm to 3.2 at 875 nm. Meanwhile, our estimation showed that $n_{\text{ef}} \approx 2$ for 700 nm and 600 nm, and 1.5 for 500 nm.

Knowing n_{ef} for a certain combination of photoresist and laser systems would lead to more comparable results obtained by different academic and applied practitioners in 3D printing/ photopolymerisation. In this study, we demonstrated that employing ultrashort pulses of 100 fs duration photopolymerisation within a wide λ range (500 – 1200 nm) is possible, while $R = 1$ MHz and $v = 100 \mu\text{m/s}$ were constant. This is markedly different from results reported for long pulse ns (Liao et al. 2007) and CW regimes (Nguyen et al. 2016; Thiel et al. 2010) photopolymerisation where precise λ has to be used (e.g. 532 nm was reported). In this study, we were not limited to only assessing the line width and height but evaluated the DFW for each λ and the behaviour of the AR within it.

The employed approach was able to precisely assess n_{ef} within the entire λ range by the best fit and the proof-of-concept was demonstrated. This research confirms that a tunable λ and τ laser source could be an efficient tool for further and deeper investigation of n_{ef} in both PI and PI-free photo-polymers.

The discussion in this section so far was about the effective process order n_{ef} , which is a result of the fit.

Equations of the fit (Section 2.7) are derived for a Gaussian beam/pulse. Hence, it was called a local fit parameter. Figure 2 shows a departure from that order parameter, which can be approximated with distinct regions following slopes $\gamma = 0.5, 1, 2$. These γ slopes show a change in energy deposition mechanism and were referred to as global parameters as discussed next.

One of the most distinct and unexpected experimental observations was a step-like increase in lateral cross-section at longer $\lambda \geq 800$ nm and larger power for resist with PI (sensitised for ~ 360 nm). The power region of increase is at pulse energy $E > 1$ nJ with slope change $\gamma \rightarrow 2$. It is instructive to estimate average intensity $I = 2E/(\pi r^2 \tau)$ at the focus for $E = 1$ nJ pulse energy of $\lambda = 1 \mu\text{m}$, $\tau = 100$ fs pulse focused with $NA = 1.4$ objective lens into the Airy disk of radius $r = 0.61\lambda/NA = 436$ nm. One finds $I = 0.334$ TW/cm². This is high intensity considering that at around ~ 1 TW/cm² there is a dielectric breakdown at different λ and $\tau = 0.1 - 0.5$ ps. The dielectric breakdown is expected to be driven by avalanche ionisation acting along other run-away mechanisms. Noteworthy is that the used $I < 10$ PW/cm² when instantaneous ionisation takes place by tunnelling which is λ -independent. The rate of avalanche ionisation scales as λ^2 . In the chosen presentation of *Size versus Power*, the effect of different fluence $F = E/(\pi r^2)$ and intensity $I = F/\tau$ at different λ is irrelevant. Since $F, I \propto \lambda^{-2}$ it is compensated for the avalanche-dominated electronic excitation due to the mentioned rate scaling as λ^2 . Hence, the step-like changes in lateral voxel size should originate from different mechanisms indicating that the photo-chemical reactions can be induced via various numbers of photons – X-photons.

We put forward here a conjecture that fast size increase of voxels, hence, energy deposition has an origin of strong electronic excitation which creates epsilon-near-zero (ENZ) conditions $\varepsilon_p \rightarrow 0$, where subscript p notifies strong free carrier (electronic) plasma formation at the focus (see Figure 6 a). The most efficient energy absorption is taking place in photo-excited material when $1 > \varepsilon_p > 0$ (breakdown). At this regime, electron density $n_e \rightarrow n_{\text{cr}}$, which defines a strongly reflective medium (plasma) with reflectance $R_r \rightarrow 1$. This transitional state from dielectric-to-metallic (plasma) is defined as Die-Met (Gamaly and Rode 2018). When the real part of $\varepsilon_p = 1$, the electron density becomes $n_e = (n_0^2 - 1)n_{\text{cr}}$, where n_0 is the refractive index of unperturbed dielectric (Gamaly and Rode 2018). It is relevant to calculate a volumetric energy density $w_d \propto \frac{n_e}{n_{\text{cr}}} F [J/\text{cm}^3]$ for the estimation of 3D photopolymerisation (Skliutas et al. 2021); e.g. for the linear growth of n_e via linear absorption *versus* fluence F , the

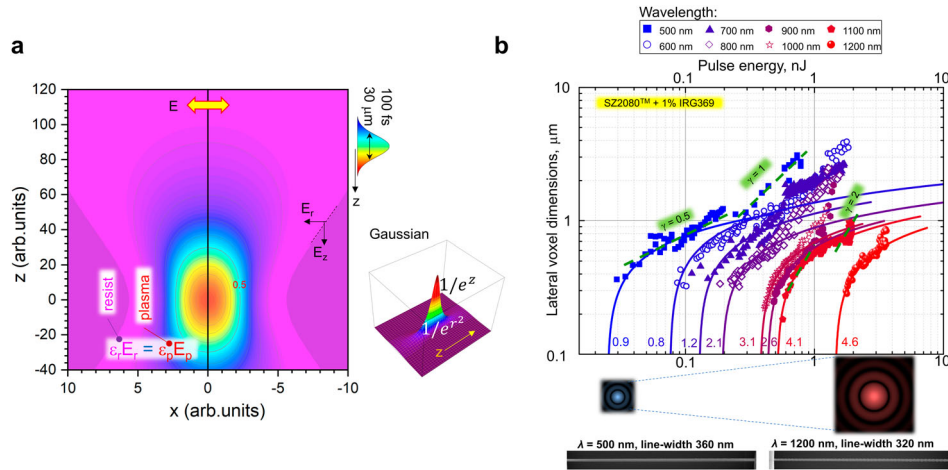


Figure 6. Energy deposition at the focus. **(a)** Gaussian intensity distribution and its axial cross-section. **(b)** Lateral voxel size evolution (same as in Figure 2) with revealed global slope γ change tendencies. The fit-obtained n_{ef} order parameter values are shown at the corresponding lines. The insets of Airy patterns are plotted to scale with λ . See text for discussion. SEM images of lines produced at 500 and 1200 nm with low powers (below diffraction limit) are depicted.

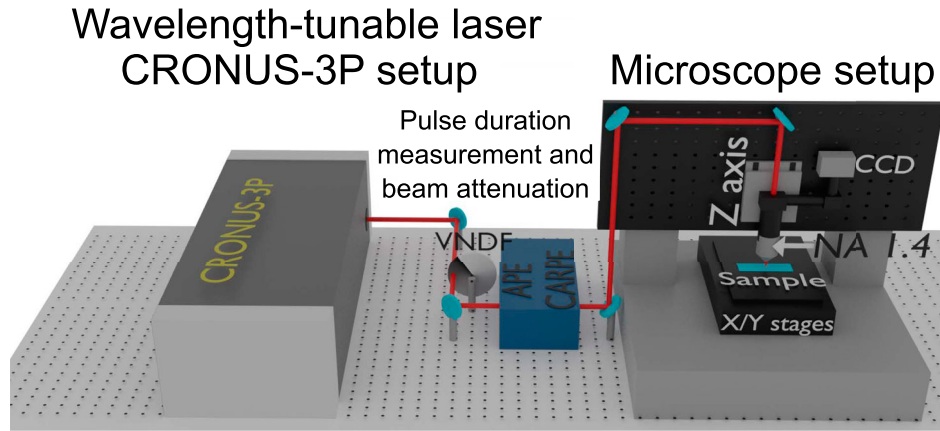


Figure 7. Experimental design. The layout of the experimental setup: tunable λ and τ laser system CRONUS-3P, τ measurement (APE CARPE) and beam attenuation control (VNDF), custom-made microscope setup: piezo-stage stack for X and Y movements, Z axis stage, focusing objective, CCD camera.

$w_d \propto F^2$ follows $\gamma = 2$ dependence. Likewise, a two-photon absorption with $n_{ef} = 2$ dependence of n_e generation rate translates to the 3D absorbed energy density $w_d \propto F^{(n_{ef}+1)} = F^3$.

Another contributing mechanism to the fast evolution of plasma density at the focus is expected due to the recently harnessed near-field enhancement used for nanolithography on dielectric nano-film (Zhen-Ze et al. 2020). The principle of larger energy deposition in the region of lower permittivity $\varepsilon \equiv \tilde{n}^2$ – the plasma region at the focus – in comparison to the surrounding resist (r -index) is shown in Figure 6(a). There the normal components of the displacements have to obey $\varepsilon_r E_r = \varepsilon_p E_p$. For intensity $I \propto E^2$, an increase at the focal (plasma) region takes place when $n_p < n_r$ as

$$\left(\frac{E_p}{E_r}\right)^2 = \left(\frac{n_r}{n_p}\right)^4, \text{ where the real parts of the refractive index } n_{p,r} \text{ at focus and surrounding resist.}$$

The described enhancement of absorption due to ENZ state formation complimented with its spatial in-homogeneity and further enhanced at the focal region via, the so-called *optical-FIB* (O-FIB, optical-focused ion beam) mechanism revealed by Sun et al (Zhen-Ze et al. 2020) (described above), which was driving the excitation at focus towards the dielectric breakdown. This behaviour is captured as a global slope change γ which is apparently λ -dependent as evidenced in Figure 6(b). The family of curves in (b) also illustrates that fs-laser pulses can be used with very controlled energy deposition even close to the run-away breakdown.

An additional important factor in enhanced energy deposition is the presence of the longitudinal E_z component, which is responsible for the resonant absorption (Juodkazis et al. 2008) (see Figure 6 a). It allows depositing more energy as compared to the paraxial E-field incidence where electronic plasma screens (reflects) incoming laser pulse. This mechanism is present at all wavelengths and contributes to the change of the global γ -slope. The most efficient energy deposition takes place close to critical plasma density which is λ dependent: $n_{cr} = m_e \epsilon_0 \omega^2 / e^2$, where m_e is the electron mass, e its charge, $\omega = 2\pi c / \lambda$ is the cyclic frequency of light and ϵ_0 is the permittivity of free space.

5. Conclusion

3D nanolithography with ultra-short $\tau \approx 100$ fs pulses at a wide visible-to-near-IR spectral range of $\lambda = 400 - 1200$ nm (a three octaves frequency span) proceeds via multi-photon excitation defined by effective order exponent $n_{ef} = 0.8 - 4.6$. The deviation of the lateral voxel size from analytical curve was observed and had a distinct step-like onset most expressed at a longer wavelength and higher power. This augmented energy deposition is consistent with ENZ state formation at the focal region which causes a larger portion of incident light intensity to be absorbed yielding a large lateral cross-section of photopolymerised voxel (line) (Joglekar et al. 2004). The validation of the approach was realised in an SZ2080™ as a model material and should be viable with other widespread materials such as commercial IP photoresins, PETA and other cross-linkable materials.

Here, we have shown that femtosecond laser 3D nanolithography can be implemented at various wavelengths and even without the need for PI. Of course, every selected wavelength and presence or absence of PI influenced DFW , revealing that lasers of various wavelengths can be optimised for specialised structuring results. For example, shorter wavelengths showed higher production throughput and lower photo-chemical energy conversion yield. This is advantageous in the MPP community, as could enable rapid paralleled multi-beam fabrication further increasing throughput. However, contrary to the literature, the efforts carried out toward reaching the highest structuring resolution did not directly reveal that some specific wavelength is advantageous for such purposes.

In perspective, deeper insights are still required into the mechanism of heat accumulation, which is dependent on scan speed and laser repetition rate, as well as

focal spot size. The tunable wavelength, together with pulse chirp, duration and burst-mode operation, which is becoming a standard in commercial fs-laser sources can provide further improvements. Considering the trend of the last 20 years of Moore's law scaling with an average fs-laser power doubling every two years (Han et al. 2021), the high-throughput applications will benefit from parameter-optimised 3D nano-printing.

Acknowledgments

We acknowledge the long-lasting interest and support of Prof. Acad. Algis P. Piskarskas in studying and developing ultrafast laser 3D nanolithography, including coining the terms *nanophotonic* and suggesting *X-photon* for the unknown multiphoton order, both of which were reflected in the title of this paper in the memory of his passing.

Data availability statement

The data that support the findings of this study are available from the corresponding author, E. S., upon reasonable request.








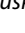
Disclosure statement

No potential conflict of interest was reported by the author(s).

Funding

This work was supported by the Research Council of Lithuania under Grant No. S-MIP-20-17 and EU Horizon 2020, Research and Innovation program LASERLAB-EUROPE JRA under Grant No. 871124.

ORCID

Edvinas Skliutas  <https://orcid.org/0000-0001-5226-2801>
 Danielius Samsonas  <https://orcid.org/0000-0001-8922-4956>
 Lukas Kontenis  <https://orcid.org/0000-0002-8856-9538>
 Darius Gailevičius  <https://orcid.org/0000-0002-1453-3276>
 Jonas Berzinš  <https://orcid.org/0000-0001-6970-1145>
 Mikas Vengris  <https://orcid.org/0000-0003-1780-5617>
 Saulius Juodkazis  <https://orcid.org/0000-0003-3542-3874>
 Mangirdas Malinauskas  <http://orcid.org/0000-0002-6937-4284>

References

- Baldacchini, T., S. Snider, and R. Zadayan. 2012. "Two-Photon Polymerization with Variable Repetition Rate Bursts of Femtosecond Laser Pulses." *Optics Express* 20 (28): 29890–29899. <https://doi.org/10.1364/OE.20.029890>.
- Blaicher, M., M. R. Billah, J. Kemal, T. Hoose, P. Marin-Palomo, A. Hofmann, and Y. Kutuvantavida. 2020. "Hybrid Multi-chip Assembly of Optical Communication Engines by In Situ 3D

- Nano-lithography." *Light: Science & Applications* 9 (1): 1–11. <https://doi.org/10.1038/s41377-020-0272-5>.
- Butkus, A., E. Skliutas, D. Gailevičius, and M. Malinauskas. 2022. "Femtosecond-laser Direct Writing 3D Micro/nano-lithography Using VIS-light Oscillator." *Journal of Central South University* 29 (10): 3270–3276. <https://doi.org/10.1007/s11771-022-5153-z>.
- DeVoe, R. J., H. W. Kalweit, C. A. Leatherdale, and T. R. Williams. 2003. "Voxel Shapes in Two-Photon Microfabrication." In *Proc. Multiphoton Absorption and Nonlinear Transmission Processes: Materials, Theory, and Applications*, edited by Kevin D. Belfield, Stephen J. Caracci, Francois Kajzar, Christopher M. Lawson, and Alan T. Yeates, Vol. 4797, 4797:310. SPIE, San Francisco.
- Do, Mai Trang, Thi Thanh Ngan Nguyen, Qinggele Li Henri Benisty, Isabelle Ledoux-Rak, and Ngoc Diep Lai. 2013. "Submicrometer 3D Structures Fabrication Enabled by One-Photon Absorption Direct Laser Writing." *Optics Express* 21 (18): 20964–20973. <https://doi.org/10.1364/OE.21.020964>.
- Dottermusch, Stephan, Dmitry Busko, Malte Langenhorst, Ulrich W. Paetzold, and Bryce S. Richards. 2019. "Exposure-dependent Refractive Index of Nanoscribe IP-Dip Photoresist Layers." *Optics Letters* 44 (1): 29–32. <https://doi.org/10.1364/OL.44.000029>.
- Fischer, Joachim, Jonathan B. Mueller, Johannes Kaschke, Thomas J. A. Wolf, Andreas-Neil Unterreiner, and Martin Wegener. 2013. "Three-dimensional Multi-photon Direct Laser Writing with Variable Repetition Rate." *Optics Express* 21 (22): 26244–26260. <https://doi.org/10.1364/OE.21.026244>.
- Fischer, Joachim, and Martin Wegener. 2013. "Three-Dimensional Optical Laser Lithography Beyond the Diffraction Limit." *Laser & Photonics Reviews* 7 (1): 22–44. <https://doi.org/10.1002/lpor.201100046>.
- Flamourakis, George, Ioannis Spanos, Zacharias Vangelatos, Phanee Manganas, Lina Papadimitriou, Costas Grigoropoulos, Anthi Ranella, and Maria Farsari. 2020. "Laser-made 3D Auxetic Metamaterial Scaffolds for Tissue Engineering Applications." *Macromolecular Materials and Engineering* 305 (7): 2000238. <https://doi.org/10.1002/mame.v305.7>.
- Fu, Hongxun, Xian Jing, Jieqiong Lin, Liye Wang, Hancheng Jiang, and Baojun Yu Meiyan Sun. 2022. "Knowledge Domain and Hotspots Analysis Concerning Applications of Two-Photon Polymerization in Biomedical Field: A Bibliometric and Visualized Study." *Frontiers in Bioengineering and Biotechnology* 10:1030377. <https://doi.org/10.3389/fbioe.2022.1030377>.
- Gailevičius, D., V. Padolskytė, S. Šakirzanovas, S. Juodkasis, and M. Malinauskas. 2019. "Additive-manufacturing of 3D Glass-ceramics Down to Nanoscale Resolution." *Nanoscale Horizons* 4 (3): 647–651. <https://doi.org/10.1039/C8NH00293B>.
- Gamaly, E. G., and A. V. Rode. 2018. "Ultrafast Re-structuring of the Electronic Landscape of Transparent Dielectrics: New Material States (Die-Met)." *Applied Physics A* 124 (3): 278. <https://doi.org/10.1007/s00339-018-1693-3>.
- Gan, Zongsong, Yaoyu Cao, Richard-A. Evans, and Min Gu. 2013. "Three-Dimensional Deep Sub-diffraction Optical Beam Lithography with 9 Nm Feature Size." *Nature Communications* 4 (1): 2061. <https://doi.org/10.1038/ncomms3061>.
- Guney, M. G., and G. K. Fedder. 2016. "Estimation of Line Dimensions in 3D Direct Laser Writing Lithography." *Journal of Micromechanics and Microengineering* 26 (10): 105011. <https://doi.org/10.1088/0960-1317/26/10/105011>.
- Hahn, Vincent, Pascal Kiefer, Tobias Frenzel, Jingyuan Qu Eva Blasco, Christopher Barner-Kowollik, and Martin Wegener. 2020. "Rapid Assembly of Small Materials Building Blocks (Voxels) into Large Functional 3D Metamaterials." *Advanced Functional Materials* 30 (26): 1907795. <https://doi.org/10.1002/adfm.v30.26>.
- Hahn, Vincent, Tobias Messer, N. Maximilian Bojanowski, Ernest Ronald Curticean, Irene Wacker, Rasmus R. Schröder, Eva Blasco, and Martin Wegener. 2021. "Two-step Absorption Instead of Two-photon Absorption in 3D Nanoprinting." *Nature Photonics* 15 (12): 932–938. <https://doi.org/10.1038/s41566-021-00906-8>.
- Han, Molong, Daniel Smith, Soon-Hock Ng Vijayakumar Anand, and Saulius Juodkasis. 2021. "Ultra-Short-Pulse Lasers-Materials-Applications." *Engineering Proceedings* 11 (1):44. <https://doi.org/10.3390/ASEC2021-11143>.
- Horváth, Bence, Pál Ormos, and Lóránd Kelemen. 2017. "Nearly Aberration-Free Multiphoton Polymerization Into Thick Photoresist Layers." *Micromachines* 8 (7): 219. <https://doi.org/10.3390/mi8070219>.
- Joglekar, Ajit P., Hsiao Hua Liu, Edgar Meyhöfer, Gerard Mourou, and Alan J. Hunt. 2004. "Optics at Critical Intensity: Applications to Nanomorphing." *Proceedings of the National Academy of Sciences of the United States of America* 101 (16): 5856–5861. <https://doi.org/10.1073/pnas.0307470101>.
- Johnson, Jason E., and Xianfan Xu Yijie Chen. 2022. "Model for Polymerization and Self-deactivation in Two-photon Nanolithography." *Optics Express* 30 (15): 26824–26840. <https://doi.org/10.1364/OE.461969>.
- Jonušauskas, Linas, Darius Gailevičius, Sima Reškūtytė, Tommaso Baldacchini, Saulius Juodkasis, and Mangirdas Malinauskas. 2019. "Mesoscale Laser 3D Printing." *Optics Express* 27 (11): 15205–15221. <https://doi.org/10.1364/OE.27.015205>.
- Joye, W. A., and E. Mandel. 2003. "New Features of SAOImage DS9." In *Proc. Astronomical Data Analysis Software and Systems XII*, edited by H. E. Payne, R. I. Jedrzejewski, and R. N. Hook, Vol. 295 of *Astronomical Society of the Pacific Conference Series*, 489.
- Juodkasis, Saulius, Vyantas Mizeikis, Kock Khuen Seet, Masafumi Miwa, and Hiroaki Misawa. 2005. "Two-Photon Lithography of Nanorods in SU-8 Photoresist." *Nanotechnology* 16 (6): 846–849. <https://doi.org/10.1088/0957-4484/16/6/039>.
- Juodkasis, Saulius, Mizeikis Vyantas, Matsuo Shigeki, Ueno Kosei, and Misawa Hiroaki. 2008. "Three-Dimensional Micro- and Nano-Structuring of Materials by Tightly Focused Laser Radiation." *Bulletin of the Chemical Society of Japan* 81 (4): 411–448. <https://doi.org/10.1246/bcsj.81.411>.
- Kawata, Satoshi, Hong-Bo Sun, Tomokazu Tanaka, and Kenji Takada. 2001. "Finer Features for Functional Microdevices." *Nature* 412 (6848): 697–698. <https://doi.org/10.1038/35089130>.
- Ketchum, R. S., P. E. Alcaraz, and P.-A. Blanche. 2022. "Modified Photoresins with Tunable Refractive Index for 3D Printed Micro-optics." *Optical Materials Express* 12 (8): 3152–3160. <https://doi.org/10.1364/OME.464630>.

- Kiefer, Pascal, Vincent Hahn, Martina Nardi, Liang Yang, Eva Blasco, Christopher Barner-Kowollik, and Martin Wegener. 2020. "Sensitive Photoresists for Rapid Multiphoton 3D Laser Micro- and Nanoprinting." *Advanced Optical Materials* 8 (19): 1–14. <https://doi.org/10.1002/adom.v8.19>.
- Ladika, D., G. Noirbent, F. Dumur, D. Gigmes, A. Mourka, G. D. Barmparis, M. Farsari, and D. Gray. 2022. "Synthesis and Application of Triphenylamine-based Aldehydes as Photoinitiators for Multiphoton Lithography." *Applied Physics A* 128 (9): 745. <https://doi.org/10.1007/s00339-022-05887-1>.
- LaFratta, Christopher N., and Tommaso Baldacchini. 2017. "Two-photon Polymerization Metrology: Characterization Methods of Mechanisms and Microstructures." *Micromachines* 8 (4): 101. <https://doi.org/10.3390/mi8040101>.
- Lemma, Enrico Domenico, Francesco Rizzi, Tommaso Dattoma, Barbara Spagnolo, Leonardo Sileo, Antonio Quattieri, Massimo De Vittorio, and Ferruccio Pisanello. 2017. "Mechanical Properties Tunability of Three-Dimensional Polymeric Structures in Two-Photon Lithography." *IEEE Transactions on Nanotechnology* 16 (1): 23–31. <https://doi.org/10.1109/TNANO.2016.2625820>.
- Liao, Chao Yaug, Michel Bouriaudand, Patrice L. Baldeck, Jean Claude Lon, Ćdric Masclat, and Tien Tung Chung. 2007. "Two-dimensional Slicing Method to Speed Up the Fabrication of Micro-objects Based on Two-photon Polymerization." *Applied Physics Letters* 91 (3): 033108. <https://doi.org/10.1063/1.2759269>.
- Liaros, Nikolaos, and John T. Fourkas. 2021. "Methods for Determining the Effective Order of Absorption in Radical Multiphoton Photoresists: A Critical Analysis." *Laser & Photonics Reviews* 15 (1): 2000203. <https://doi.org/10.1002/lpor.v15.1>.
- Liu, Yejing, Hao Wang, Jinfa Ho, Ryan C. Ng, Ray J. H. Ng, Valerian H. Hall-Chen, and Eleen H. H. Koay. 2019. "Structural Color Three-dimensional Printing by Shrinking Photonic Crystals." *Nature Communications* 10 (1): 4340. <https://doi.org/10.1038/s41467-019-12360-w>.
- Lunzer, M., Joseph S. Beckwith, F. Chalupa-Gantner, A. Rosspeintner, G. Licari, W. Steiger, and C. Hametner. 2022. "Beyond the Threshold: A Study of Chalcogenophene-Based Two-Photon Initiators." *Chemistry of Materials* 34 (7): 3042–3052. <https://doi.org/10.1021/acs.chemmater.1c04002>.
- Münchinger, A., L.-Y. Hsu, F. Fűrniß, E. Blasco, and M. Wegener. 2022. "3D Optomechanical Metamaterials." *Materials Today* 59:9–17. <https://doi.org/10.1016/j.mattod.2022.08.020>.
- Malinauskas, Mangirdas, Paulius Danilevičius, and Saulius Juodkazis. 2011. "Three-dimensional Micro-/nano-structuring Via Direct Write Polymerization with Picosecond Laser Pulses." *Optics Express* 19 (6): 5602–5610. <https://doi.org/10.1364/OE.19.005602>.
- Malinauskas, M., V. Purlys, M. Rutkauskas, and R. Gadonas. 2010. "Femtosecond Visible Light Induced Two-photon Photopolymerization for 3D Micro/nanostructuring in Photoresists and Photopolymers." *Lithuanian Journal of Physics* 50 (2): 201–207. <https://doi.org/10.3952/lithjphys.50203>.
- Malinauskas, M., A. Žukauskas, G. Bičkauskaitė, R. Gadonas, and S. Juodkazis. 2010. "Mechanisms of Three-dimensional Structuring of Photo-polymers by Tightly Focussed Femtosecond Laser Pulses." *Optics Express* 18 (10): 10209–10221. <https://doi.org/10.1364/OE.18.010209>.
- Marble, Christopher B., Kassie S. Marble, and Vladislav V. Yakovlev. 2020. "Nanoscale Optical Assessment of Photochemical Changes of SU-8 Photoresist Induced by Ultrashort Near-IR Optical Excitation." *Applied Physics A: Materials Science and Processing* 126 (10): 1–6. <https://doi.org/10.1007/s00339-020-03991-8>.
- Maruo, Shoji, Osamu Nakamura, and Satoshi Kawata. 1997. "Three-dimensional Microfabrication with Two-Photon-Absorbed Photopolymerization." *Optics Letters* 22 (2): 132–134. <https://doi.org/10.1364/OL.22.000132>.
- Mckee, Seyyedhossien, Adrian Lutey, Corrado Sciancalepore, Federica Poli, Stefano Selleri, and Annamaria Cucinotta. 2022. "Microfabrication of Polymer Microneedle Arrays Using Two-photon Polymerization." *Journal of Photochemistry and Photobiology B: Biology* 229:112424. <https://doi.org/10.1016/j.jphotobiol.2022.112424>.
- McLennan, H. J., A. J. Blanch, S. J. Wallace, L. J. Ritter, S. L. Heinrich, D. K. Gardner, and K. R. Dunning. 2023. "Nanoliter Perfusion Microfluidic Device Made Entirely by Two-photon Polymerization for Dynamic Cell Culture with Easy Cell Recovery." *Scientific Reports* 13 (1): 1–16. <https://doi.org/10.1038/s41598-023-27660-x>.
- Merkininkaitė, G., E. Aleksandravičius, M. Malinauskas, D. Gailevičius, and S. Šakirzanovas. 2022. "Laser Additive Manufacturing of Si/ZrO₂ Tunable Crystalline Phase 3D Nanostructures." *Opto-Electronic Advances* 5 (5): 210077–210077. <https://doi.org/10.29026/oea.2022.210077>.
- Miwa, M., S. Juodkazis, T. Kawakami, S. Matsuo, and H. Misawa. 2001. "Femtosecond Two-photon Stereo-lithography." *Applied Physics A: Materials Science and Processing* 73 (5): 561–566. <https://doi.org/10.1007/s003390100934>.
- Mueller, J. B., J. Fischer, F. Mayer, M. Kadic, and M. Wegener. 2014. "Polymerization Kinetics in Three-Dimensional Direct Laser Writing." *Advanced Materials* 26 (38): 6566–6571. <https://doi.org/10.1002/adma.v26.38>.
- Mueller, P., M. Thiel, and M. Wegener. 2014. "3D Direct Laser Writing Using a 405 Nm Diode Laser." *Optics Letters* 39 (24): 6847–6850. <https://doi.org/10.1364/OL.39.006847>.
- Mueller, P., M. M. Zieger, B. Richter, A. S. Quick, J. Fischer, J. B. Mueller, and L. Zhou. 2017. "Molecular Switch for Sub-Diffraction Laser Lithography by Photoenol Intermediate-State Cis-Trans Isomerization." *ACS Nano* 11 (6): 6396–6403. <https://doi.org/10.1021/acsnano.7b02820>.
- Nguyen, D. T. T., Q. C. Tong, I. Ledoux-Rak, and N. D. Lai. 2016. "One-step Fabrication of Submicrostructures by Low One-photon Absorption Direct Laser Writing Technique with Local Thermal Effect." *Journal of Applied Physics* 119 (1): 013101. <https://doi.org/10.1063/1.4939294>.
- Obata, K., F. C. Lucas, and K. Sugioka. 2022. "Multi-Photon Polymerization by GHz Burst Mode Femtosecond Laser Pulses for Improvement of Process Resolution." In *Proc. Laser Applications in Microelectronic and Optoelectronic Manufacturing (LAMOM) XXVII*, edited by Kevin D. Belfield, Stephen J. Caracci, Francois Kajzar, Christopher M. Lawson, and Alan T. Yeates, Vol. PC11988, PC1198803. SPIE, San Francisco.
- Ovsianikov, A., J. Viertel, B. Chichkov, M. Oubaha, B. Maccraith, I. Sakellari, and A. Giakoumaki. 2008. "Ultra-Low Shrinkage Hybrid Photosensitive Material for Two-Photon Polymerization Microfabrication." *ACS Nano* 2 (11): 2257–2262. <https://doi.org/10.1021/nn800451w>.
- Peek, S. E., J. Ward, S. Bankson, A. Shah, J. A. Sellers, M. L. Adams, and M. C. Hamilton. 2022. "Additive Manufacturing

- and Characterization of Microstructures Using Two-photon Polymerization for Use in Cryogenic Applications." *Journal of Materials Research* 37 (12): 1978–1985. <https://doi.org/10.1557/s43578-022-00610-5>.
- Perevozniĳ, D., R. Nazir, R. Kiyān, K. Kurselis, B. Koszarna, D. T. Gryko, and B. N. Chichkov. 2019. "High-speed Two-photon Polymerization 3D Printing with a Microchip Laser at Its Fundamental Wavelength." *Optics Express* 27 (18): 25119–25125. <https://doi.org/10.1364/OE.27.025119>.
- Saha, S. K., C. Divin, J. A. Cuadra, and R. M. Panas. 2017. "Effect of Proximity of Features on the Damage Threshold During Submicron Additive Manufacturing Via Two-photon Polymerization." *Journal of Micro and Nano-Manufacturing* 5 (3): 031002. <https://doi.org/10.1115/1.4036445>.
- Saha, S. K., D. Wang, V. H. Nguyen, Y. Chang, J. S. Oakdale, and S. C. Chen. 2019. "Scalable Submicrometer Additive Manufacturing." *Science* 366 (6461): 105–109. <https://doi.org/10.1126/science.aax8760>.
- Samsonas, D., E. Skliutas, A. Čiburyš, L. Kontenis, D. Gailevičius, J. Berziš, and D. Narbutis. 2023. "3D Nanopolymerization and Damage Threshold Dependence on Laser Wavelength and Pulse Duration." *Nanophotonics* 12 (8): 1537–1548. <https://doi.org/10.1515/nanoph-2022-0629>.
- Sandford O'Neill, J., P. Salter, Z. Zhao, B. Chen, H. Dagainawalla, M. J. Booth, S. J. Elston, and S. M. Morris. 2022. "3D Switchable Diffractive Optical Elements Fabricated with Two-Photon Polymerization." *Advanced Optical Materials* 10 (7): 2102446. <https://doi.org/10.1002/adom.v10.7>.
- Skliutas, E., M. Lebedevaite, E. Kabouraki, T. Baldacchini, J. Ostrauskaite, M. Vamvakaki, M. Farsari, S. Juodkazis, and M. Malinauskas. 2021. "Polymerization Mechanisms Initiated by Spatio-temporally Confined Light." *Nanophotonics* 10 (4): 1211–1242. <https://doi.org/10.1515/nanoph-2020-0551>.
- Somers, P., Z. Liang, J. E. Johnson, B. W. Boudouris, L. Pan, and X. Xu. 2021. "Rapid, Continuous Projection Multi-photon 3D Printing Enabled by Spatiotemporal Focusing of Femtosecond Pulses." *Light: Science & Applications* 10 (1): 1–11. <https://doi.org/10.1038/s41377-021-00645-z>.
- Stankevičius, E., E. Daugnoraitė, and G. Račiukaitis. 2018. "Photopolymerization Differences by Using Nanosecond and Picosecond Laser Pulses." *Optics Express* 25 (5): 4819–4830. <https://doi.org/10.1364/OE.25.004819>.
- Sun, H. B., K. Takada, M. S. Kim, K. S. Lee, and S. Kawata. 2003. "Scaling Laws of Voxels in Two-photon Photopolymerization Nanofabrication." *Applied Physics Letters* 83 (6): 1104–1106. <https://doi.org/10.1063/1.1599968>.
- Thiel, M., J. Fischer, G. Von Freymann, and M. Wegener. 2010. "Direct Laser Writing of Three-dimensional Submicron Structures Using a Continuous-wave Laser at 532 Nm." *Applied Physics Letters* 97 (22): 221102. <https://doi.org/10.1063/1.3521464>.
- Tomova, Z., N. Liaros, S. A. Gutierrez Razo, S. M. Wolf, and J. T. Fourkas. 2016. "In Situ Measurement of the Effective Nonlinear Absorption Order in Multiphoton Photoresists." *Laser & Photonics Reviews* 10 (5): 849–854. <https://doi.org/10.1002/lpor.v10.5>.
- Vyatskikh, A., S. Delalande, A. Kudo, X. Zhang, C. M. Portela, and J. R. Greer. 2018. "Additive Manufacturing of 3D Nano-architected Metals." *Nature Communications* 9 (1): 1–8. <https://doi.org/10.1038/s41467-018-03071-9>.
- Williams, H. E., C. Diaz, G. Padilla, F. E. Hernandez, and S. M. Kuebler. 2017. "Order of Multiphoton Excitation of Sulfonium Photo-acid Generators Used in Photoresists Based on SU-8." *Journal of Applied Physics* 121 (22): 223104. <https://doi.org/10.1063/1.4984828>.
- Yang, L., H. Hu, A. Scholz, F. Feist, G. C. Marques, S. Kraus, and N. M. Bojanowski. 2023. "Laser Printed Microelectronics." *Nature Communications* 14 (1): 1–10. <https://doi.org/10.1038/s41467-022-34464-6>.
- Yang, L., A. Münchinger, M. Kadic, V. Hahn, F. Mayer, E. Blasco, C. Barner-Kowollik, and M. Wegener. 2019. "On the Schwarzschild Effect in 3D Two-Photon Laser Lithography." *Advanced Optical Materials* 7 (22): 1901040. <https://doi.org/10.1002/adom.v7.22>.
- Zhang, Y. L., Y. Tian, H. Wang, Z. C. Ma, D. D. Han, L. G. Niu, Q. D. Chen, and H. B. Sun. 2019. "Dual-3D Femtosecond Laser Nanofabrication Enables Dynamic Actuation." *ACS Nano* 13 (4): 4041–4048. <https://doi.org/10.1021/acsnano.8b08200>.
- Zhang, W., H. Wang, A. T. L. Tan, A. S. Ranganath, B. Zhang, H. Wang, and J. Y. E. Chan. 2022. "Stiff Shape Memory Polymers for High-Resolution Reconfigurable Nanophotonics." *Nano Letters* 22 (22): 8917–8924. <https://doi.org/10.1021/acs.nanolett.2c03007>.
- Zhen-Ze, L., W. Lei, F. Hua, Y. Yan-Hao, C. Qi-Dai, J. Saulius, and S. Hong-Bo. 2020. "O-FIB: Far-field-induced Near-field Breakdown for Direct Nanowriting in an Atmospheric Environment." *Light: Science and Applications* 9 (1): 41. <https://doi.org/10.1038/s41377-020-0275-2>.
- Zyla, G., A. Kovalev, C. Esen, A. Ostendorf, and S. Gorb. 2022. "Two-Photon Polymerization as a Potential Manufacturing Tool for Biomimetic Engineering of Complex Structures Found in Nature." *Journal of Optical Microsystems* 2 (03): 031203. <https://doi.org/10.1117/1.JOM.2.3.031203>.
- Zyla, G., N. Surkamp, E. L. Gurevich, E. L. Gurevich, C. Esen, A. Klehr, A. Knigge, M. R. Hofmann, and A. Ostendorf. 2020. "Two-photon Polymerization with Diode Lasers Emitting Ultrashort Pulses with High Repetition Rate." *Optics Letters* 45 (17): 4827–4830. <https://doi.org/10.1364/OL.401738>.